Giant Tunneling Piezoresistance of Composite Elastomers with Interlocked Microdome Arrays for Ultrasensitive and Multimodal Electronic Skins

Jonghwa Park,[†] Youngoh Lee,[†] Jaehyung Hong,[‡] Minjeong Ha,[†] Young-Do Jung,[§] Hyuneui Lim,[§] Sung Youb Kim,[‡] and Hyunhyub Ko[†,*]

[†]School of Energy and Chemical Engineering, Ulsan National Institute of Science and Technology (UNIST), Ulsan Metropolitan City, 689-798, Republic of Korea, [‡]School of Mechanical and Advanced Materials Engineering, Ulsan National Institute of Science and Technology (UNIST), Ulsan Metropolitan City, 689-798, Republic of Korea, and [§]Department of Nature-Inspired Nanoconvergence Systems, Korea Institute of Machinery & Materials, Daejeon, 305-343, Republic of Korea

ABSTRACT The development of flexible electronic skins with high sensitivities and multimodal sensing capabilities is of great interest for applications ranging from human healthcare monitoring to robotic skins to prosthetic limbs. Although piezoresistive composite elastomers have shown great promise in this area of research, typically poor sensitivities and low response times, as well as signal drifts with temperature, have prevented further development of these materials in electronic skin applications. Here, we introduce and demonstrate a design of flexible electronic skins based on composite elastomer films that contain interlocked microdome arrays and display giant tunneling piezoresistance. Our design substantially increases the change in contact area upon loading and enables an extreme resistance-switching behavior (R_{OFF}/R_{ON} of $\sim 10^5$). This translates into high sensitivity to pressure (-15.1 kPa^{-1}, $\sim$0.2 Pa minimum detection) and rapid response/relaxation times ($\sim$0.04 s), with a minimal dependence on temperature variation. We show that our sensors can sensitively monitor human breathing flows and voice vibrations, highlighting their potential use in wearable human-health monitoring systems.

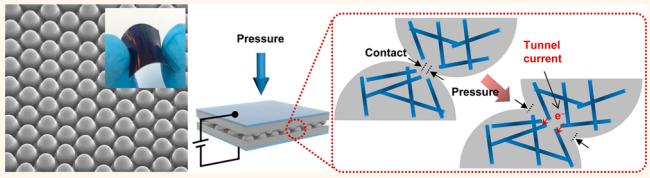

KEYWORDS: flexible electronic skin · tunneling piezoresistance · carbon nanotube composite · tactile sensor · human-health monitoring system

Human skin possesses a high degree of flexibility and stretchability and can sense pressure, shear, strain, temperature, humidity, fluid flow, and pain. As such, it is an ideal system to model multifunctional and flexible electronic skins,[1,2] which are used in wearable electronics, prosthetic limbs, robotic skins, and remote surgery, as well as in a wide range of other electronic and biomedical applications.[3−15] Proposed and implemented approaches for realizing flexible and sensitive electronic skins include systems based on resistive,[4,5,8,10,11,13,14] capacitive,[6,9,15] piezoelectric,[12,16] and triboelectric[17] modes of operation. Although such systems have yielded performances that satisfy or exceed the sensing capabilities of human skin, the development of flexible electronic skins that possess multimodal sensing capabilities for the detection of subtle environment changes remains challenging.

Piezoresistive composite elastomers hold substantial promise for the realization of electronic skins, owing to their inherent flexibility, stretchability, and chemical stability and simple, scalable, and low-cost fabrication processes. Traditionally, conductive fillers such as carbon blacks, graphites, metal particles, and carbon nanotubes (CNTs) are incorporated into elastomers to generate piezoresistive behavior. The piezoresistivities are primarily attributed to the variation in tunneling resistance when the interfiller

* Address correspondence to hyunhko@unist.ac.kr.

Received for review January 22, 2014 and accepted March 4, 2014.

Published online March 04, 2014
10.1021/nn500441k

distance changes under external stress.[18−20] To maximize these piezoresistive effects, the concentration of conductive fillers is kept near the percolation threshold; under external stress, the resistance then changes sharply. However, sensors that are based on composite elastomers suffer from poor sensitivities and are not suitable for detection in low-pressure regimes (<∼10 kPa). Moreover, they exhibit negative effects under temperature variation, due to polymer swelling and changes in interfiller distances.[21,22] Finally, the intrinsic viscoelastic properties of composite elastomers result in significant hysteresis and slow response/relaxation times,[23] which present a significant challenge for their applications in high-performance electronic skins. In this study, we demonstrate a novel design for conventional piezoresistive composite films that overcomes many of the shortcomings listed above.

RESULTS AND DISCUSSION

Composite Elastomer Films with Interlocked Microdome Arrays. The defining feature of our design is that we shape the composite elastomer films into interlocked microdome arrays. These films were fabricated by micromolding a liquid mixture composed of CNTs, polydimethylsiloxane (PDMS) prepolymer, and a curing agent with a microhole-patterned silicon mold (Figure 1a). The micromolding process produces a flexible composite film with regular microdome arrays, characterized by a height of ∼3 μm, a diameter of ∼4 μm, and a pitch of 6 μm (Figure 1b). For the fabrication of electronic skins, two composite films with microdome arrays are combined with the patterned sides facing each other. This construction produces an interlocked geometry of microdome arrays (Figure 1c). The basic working principles of our electronic skins are illustrated in Figure 1d. The external pressure induces stress concentrations at the small contact spots and local deformations in the microdomes. In turn, the contact area between the interlocked microdome arrays increases significantly and affects the tunneling resistance at the contact spots. The result is a giant tunneling piezoresistance in the flexible films.

Performance of the Pressure Sensor. To demonstrate and quantify the effects of the interlocked geometry

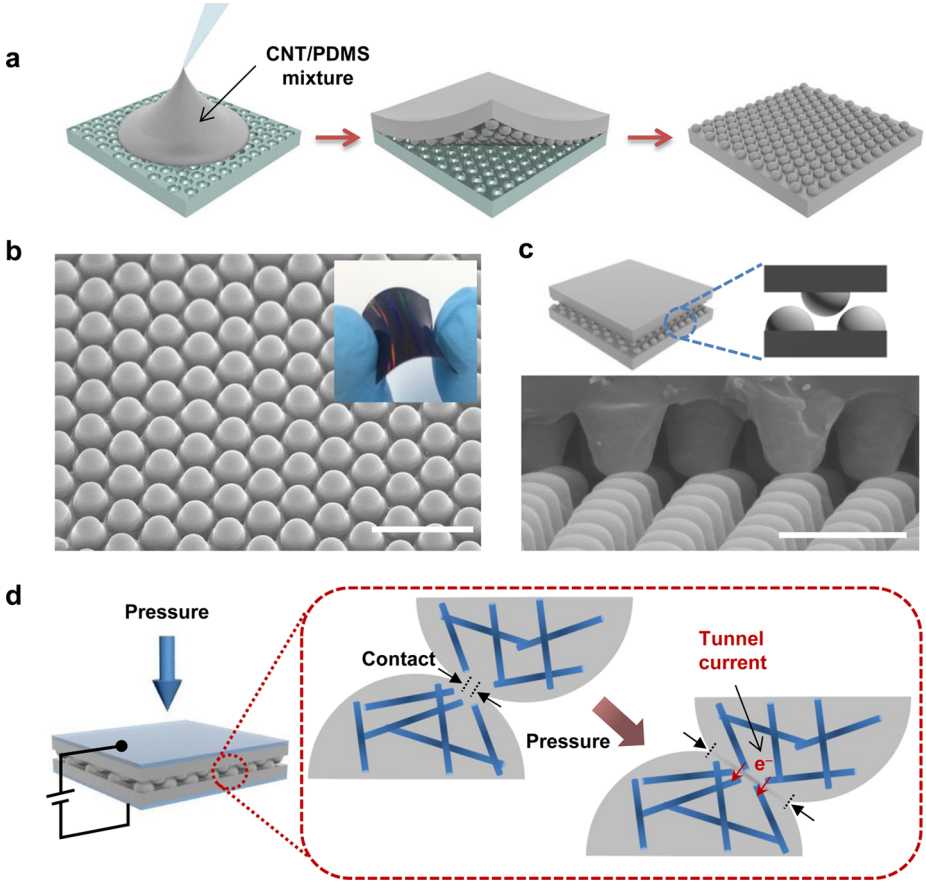

Figure 1. Conductive composite elastomers with interlocked microdome arrays. (a) Schematic of the fabrication procedure used to produce the CNT−composite elastomers with microdome arrays. (b) Tilted SEM image of the composite elastomers (bottom diameter: ∼5 μm; height: ∼3.5 μm; pitch: 6 μm). The inset photo highlights the flexibility of the arrays (scale bar: 10 μm). (c) Schematic (top) and cross-sectional SEM image (bottom) of the composite films (scale bar: 5 μm). (d) Schematic showing the working principle of the electronic skin. The external pressure concentrates stress at the contact spots, deforming the microdomes, which in turn causes an increase in the contact area and the tunneling currents.

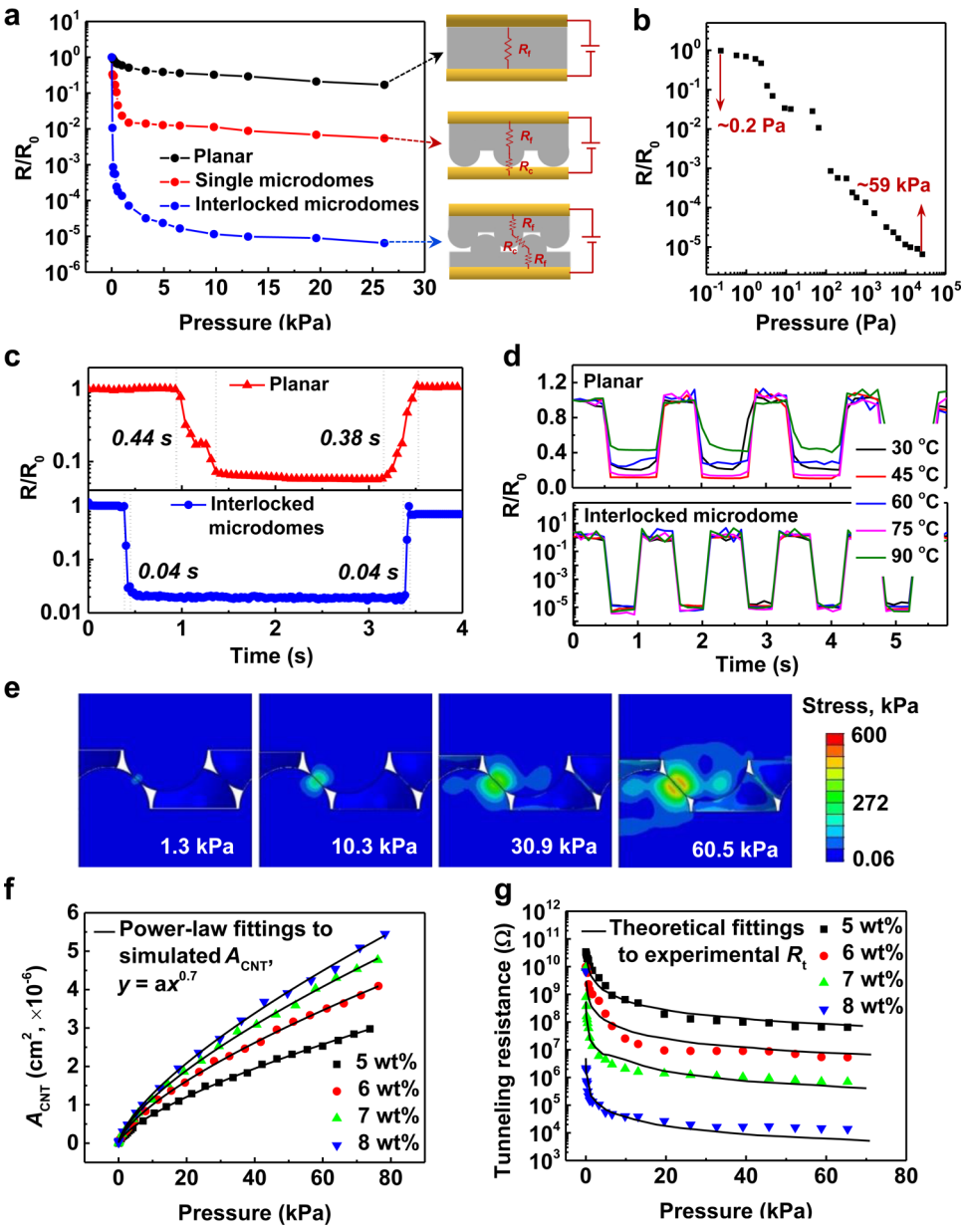

Figure 2. Pressure-sensing capabilities of sensors with interlocked microdome arrays. (a) The comparison of pressure sensitivities of different sensor structures for 8 wt % CNTs: planar (black), microdome (red), and interlocked microdome (blue). (b) Log−log plot of the pressure−response curve for the interlocked microdome arrays (8 wt % CNTs), which shows the minimum detection limit (~0.2 Pa) and the dynamic pressure range. (c) Comparison of response/relaxation times for different sensor structures for 8 wt % CNTs and 65 Pa pressure loading: planar (upper) and interlocked microdome structures (bottom). (d) Effect of temperature variation on different sensor structures for 8 wt % CNTs and 19.6 kPa pressure loading: planar (upper) and interlocked microdome structures (bottom). (e) Finite-element calculations that show the deformation and the local stress distribution of interlocked microdome arrays with applied pressure (1.3−60.5 kPa). (f) The electrical contact area (A_{CNT}) as a function of pressure for different CNT wt % (5−8 wt %). A_{CNT} is estimated by considering the CNT areal fraction in the geometrical contact area, which is obtained by using FEM simulation (Supporting Section S1). The solid lines represent power-law fits to A_{CNT} with an exponent of 0.7. (g) Experimental tunneling resistances (dotted plots) of the interlocked microdome arrays for different CNT concentrations (5−8 wt %) fitted to calculated tunneling resistances (solid lines).

on piezoresistance, we compared the electrical resistances of composite films for three different configurations: a single planar array, a single microdome array, and an interlocked microdome array (Figure S1a). All the systems with different configurations display a decrease in resistance as the pressure is increased. However, initial resistances (R_0) without applied pressures show significantly different values depending on configurations (1.4×10^4, 3.5×10^5, and 3.9×10^9 Ω for planar, single microdome, and interlocked microdomes, respectively) mainly due to the initial contact resistances. Figure 2a shows the relative electrical resistances (R/R_0) of composite films for different configurations. Composite films with interlocked microdome arrays exhibit an abrupt switching behavior with R_{OFF}/R_{ON} ratios on the order of 10^5 when the applied

pressure is increased from 0 to ~10 kPa. For composite films with single microdome arrays and composite films with planar structures, the ratio R_{OFF}/R_{ON} is ~100 and ~2, respectively. All these systems display a decrease in resistance as the pressure is increased. A switching ratio of 10^5 in a low-pressure range (<~10 kPa) compares favorably with the pressure-induced switching ratios in a high-pressure range achieved with piezoresistive composites (~10^6 at ~1 MPa)[24] and rare-earth chalcogenide films (~10^3 at ~2 GPa).[25] We attribute the significant decrease in resistance of the interlocked microdome arrays relative to the planar film primarily to the deformation of the microdome structures and the resulting variation in contact area, which affects the contact resistance (R_c) between the microdome arrays. Conversely, the piezoresistance of planar films is mainly affected by the change in film resistance (R_f) due to the decrease in intertube distances in the CNT conductive network within the composite film. We also note that the strong piezoresistive-switching behavior causes a nonlinear dependence of the resistance on pressure, which is in general observed for piezoresistive composites that exhibit tunneling effects.[19]

For quantitative analyses, the piezoresistive pressure sensitivity, S, is defined as $S = (\Delta R/R_0)/(\Delta P)$ in the linear regime, where R and P are the resistances of the sensors and the applied pressure, respectively. In the low-pressure range (<0.5 kPa) of the linear regime, the sensitivities of interlocked microdome films (−15.1 kPa^{-1}) are ~3 and ~24 times higher than the sensitivities of single microdome films (−5.4 kPa^{-1}) and planar films (−0.6 kPa^{-1}), respectively (see Supporting Information, Figure S1b). They are also significantly higher than the sensitivities recently reported for a resistive graphene−polyurethane sponge (0.26 kPa^{-1})[26] and capacitive microstructured films (0.84 kPa^{-1}).[15] The log−log plot (Figure 2b) of relative resistance as a function of pressure shows a linear decrease in relative resistance with an increase in pressure over a wide dynamic range (~0.2−59 000 Pa), which indicates an exponential dependence of resistance on the applied pressure. In particular, we observed that the sensors can detect a minimum applied pressure of ~0.2 Pa (Figure S2), which is below the gentle touch (~1 kPa) of human fingertips[27] and the minimum detection limits (>~1 kPa) of traditional piezoresistive composites[5] and comparable with values recently reported for resistive (5 Pa),[10] capacitive (3 Pa),[6] piezoelectric (0.1 Pa),[12] and triboelectric (0.4 Pa)[17] sensors. The high sensitivities of our sensors are also verified by monitoring the dynamic time-resolved change in relative resistance as water droplets with a weight of ~8.7 mg (corresponding to a pressure of ~0.6 Pa) continuously fall onto the electronic skins (Figure S3).

The interlocked-microdome-array design offers the advantage of rapid response and relaxation times as compared with the planar composite films. This is due to the immediate pressure-induced surface deformation of the microdomes in the interlocked geometry, resulting in rapid variation of contact area. On the other hand, the response/relaxation times of planar films are limited by the slow viscoelastic behavior of bulk composites. The films with interlocked microdome arrays exhibit response/relaxation times of ~0.04 s, which is an order of magnitude faster than the response/relaxation times of planar films (~0.38−0.44 s) (Figure 2c) and compares favorably with recent studies of other sensors (0.01−0.3 s).[10,15,28] A further advantage of the interlocked geometry is the reduced temperature dependence of the piezoresistance, which remains a challenging issue for conventional elastomeric composites, where the interfiller distances change during the thermal expansion of the composites.[22] As the tunneling resistance of our sensors depends primarily on the variation in contact area, our sensors show minimal changes in relative resistances with temperature changes in the range from 30 to 90 °C (Figure 2d). In contrast, the planar composite films show temperature-dependent variations in the relative resistances. Moreover, our electronic skins also display minimal hysteresis effects (Figure S4a) and maintain their initial resistance after 1000 loadings of ~59 kPa (Figure S4b).

Theoretical Considerations. To elucidate the working principles underlying the pressure sensitivity of our electronic skins, we calculated the tunneling resistance between the interlocked microdome arrays and compared these numbers with the experimental results. The tunneling resistance (R_t) at the contact spots between the interlocked microdome arrays is given by $R_t = (V/J)(1/A_{CNT})$, where V is the applied voltage, J is the current density through the insulating layer between the interlocked microdome arrays, and A_{CNT} is the electrical contact area through which the current passes between electrically conductive CNT portions at the surface of the interlocked microdome arrays. The current density is estimated within the so-called Simmons model (Section S1).[29] In this model, when the applied voltage is smaller than the barrier height, the current J tunneling through a thin layer of insulating material between metal electrodes is expressed as

$$J = \frac{e}{2\pi h \Delta s^2}\left[\bar{\varphi}\exp\left(-\frac{4\pi\Delta s\sqrt{2m}}{h}\sqrt{\bar{\varphi}}\right) - (\bar{\varphi}+eV)\times\exp\left(-\frac{4\pi\Delta s\sqrt{2m}}{h}\sqrt{\bar{\varphi}+eV}\right)\right]$$

where e is the elementary charge, h is Planck's constant, Δs and $\bar{\varphi}$ are the effective barrier thickness and average barrier height of the insulating layer, respectively, m is the electron mass, and V is the applied voltage.

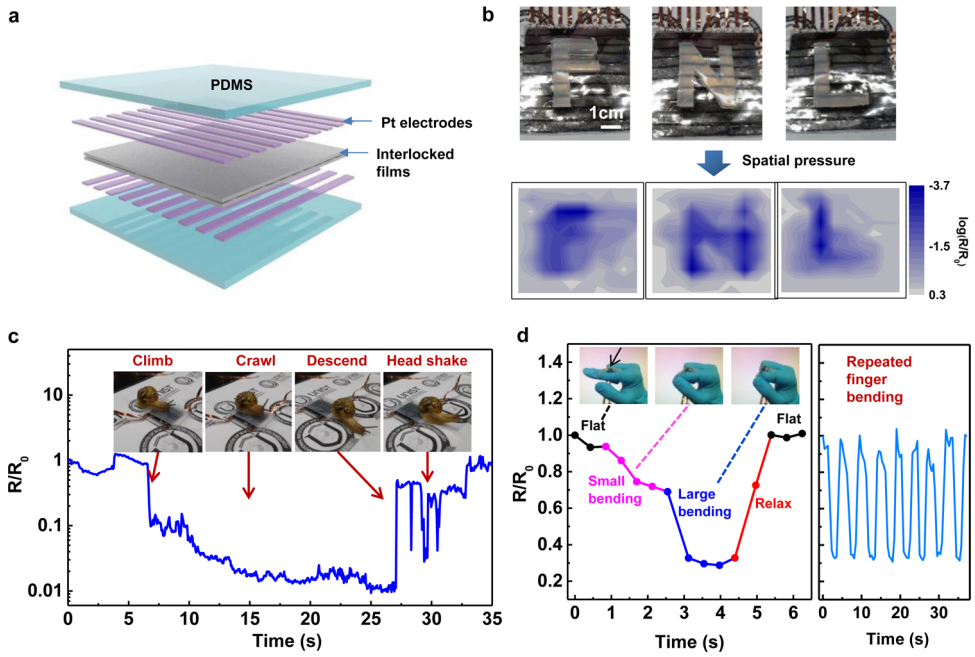

Figure 3. Sensing of spatial pressure distribution and real-time monitoring of tactile signals. (a) Schematic of the 10 × 10 sensor arrays, which consist of interlocked microdome arrays sandwiched between platinum electrodes and PDMS cover layers. (b) Spatial pressure-mapping capability of the 10 × 10 sensor arrays. The spatial pressure distribution is applied using PDMS weights that are shaped as the letters "F", "N", and "L". (c) Real-time monitoring of the change in resistance for snail movements (climb, crawl, descend, and head shake) on the surface of the electronic skins. (d) Change in resistance for different bending degrees of a finger (left) and repetitive bending cycles (right).

In order to obtain the electrical contact area (A_{CNT}) as a function of pressure, we performed finite-element simulations of a model system with interlocked microdome arrays (Section S1). As shown in Figure 2e, when pressure is applied to the electronic skin, the unique geometry of a spherical microdome induces a local-stress concentration at the small contact spots between the interlocked microdome arrays, in which the local stress field widens and the stress intensity increases with normal pressure. In particular, the local stress induces a deformation of the microdomes, which in turn causes an increase in the contact area between the interlocked microdomes (Figure S5b). The degree of increase in contact area with applied pressure depends on the elastic modulus of the microdome; the large deformation of microdomes with low elastic moduli of the composites produces a large increase in contact area. The contact area between the interlocked microdome arrays comprises the geometrical contact area (A_{dome}), which contains distributed portions of the electrical contact area (A_{CNT}). We can estimate the area A_{CNT} by considering the CNT areal fraction in the cross-sectional area of the composites (Section S1). Figure 2f shows how A_{CNT} increases with pressure, according to the power-law function $y = ax^b$ with exponent $b = 0.7$ for all samples with different CNT concentrations. This particular power-law dependence of A_{CNT} on pressure is similar to that within an analytical Hertzian contact model,[30] where $b = 2/3$. This suggests that the contact between two spheres is nonadhesive and elastic for pressures below 80 kPa. As higher CNT concentrations result in a larger CNT areal fraction, the electrical contact area increases with CNT concentration.

Experimental tunneling resistance can be expressed as $R_t = R - R_f - R_{cr}$, where R is the total resistance of the composite film (Figure S6a), R_f is the bulk-film resistance, and R_{cr} is the constriction resistance.[18] The resistance R_f is obtained from planar composite films (Figure S6b). The constriction resistance R_{cr}, which is attributed to impeded electron flow when current passes through a small contact area, can be neglected in our system, because the diameters of the CNTs and the intertube contact areas are comparable; constriction resistance can be disregarded when the ratio $D/d < \sim 10$ (where D denotes the diameter of filler material and d the diameter of the contact spot).[18] Figure 2g represents the experimental tunneling resistances, which are obtained using the equation for R_t as given above and the theoretical tunneling resistance fitted to the experimental data using an adjustable initial thickness of the insulating layer (s_0). Figure 2g shows fair agreement between the experimental data and the calculated data with an initial barrier thickness of s_0 = 15.8, 14.8, 13.5, and 11.5 Å for 5, 6, 7, and 8 wt % CNTs, respectively. We also observe that the variation in relative resistance with pressure increases with CNT concentration, due to the larger electrical contact area for higher CNT concentrations. This behavior differs distinctly from that of a planar

composite film, in which the resistance between the CNT junctions is a dominant contributor to the variation in CNT-network resistance and the composite resistance. Therefore the CNT concentration near the percolation threshold for a planar composite film (~6 wt %; Section S2 and Figure S7a) exhibits the strongest piezoresistive behavior, whereas the smallest change in resistance is observed for a concentration of 8 wt %, which exceeds the percolation threshold (Figure S7b).

Pressure Sensor Arrays and Real-Time Monitoring. In order to explore the ability of our sensors to resolve the spatial distribution and magnitude of applied pressure, we fabricated 10 × 10-pixel arrays of electronic skin sandwiched between a cross-array of platinum electrodes (Figure 3a). Pressures of 1−2 kPa were applied to the sensors *via* three different pieces of PDMS (shaped to form the letters "F", "N", and "L") placed on top of the sensor array (Figure 3b). The contact regions under the PDMS letters were compressed due to the local pressure, resulting in decreased resistance in those regions, differentiating these regions from the uncompressed regions. In addition to detecting the static-pressure distributions, our sensors were also used to detect dynamic pressure variations, which is important for real-time monitoring of environmental changes. Figure 3c shows the real-time variation in relative resistance under continuous locomotions (climb, crawl, descend, and head shake) of a live snail weighing ~540 mg. The resistance directly responded to the movement of the snail on top of the electronic skin (Movie S1). This real-time monitoring capability can also be used to monitor human motion, for example, finger-bending motion (Figure 3d). The relative resistance decreases in response to changes in finger bending and consistently changes for repeated bending cycles (Movie S2).

Human-Health Monitoring. The analysis of human-breathing patterns provides a noninvasive and repeatable monitoring technology that can be used in a variety of healthcare applications.[31] Traditionally, thermal flow sensors have been used to study human breath for the purpose of screening for cardiovascular diseases[32] or to monitor sleep apnea−hyponea syndrome.[33] However, these sensors consume a large amount of power (>0.1−1 W) and are therefore not suitable for integration into flexible electronic skins. The ability to sensitively detect applied pressure makes our sensors well suited to monitoring breathing rates. As schematically shown in Figure 4a, gas flow on the electronic skin's surface can impart normal pressures that deform the interlocked microdome arrays and cause a decrease in resistance. This change in electrical resistance ($R_{off} - R_{on}$) of the interlocked microdome arrays increases linearly with an increase in gas-flow rate (1−6 m/s); the slope indicates flow sensitivity (ΔR/m/s) of 1280 Ω/m/s (Figure 4a). Conversely, the planar composite films exhibit a flow sensitivity of only

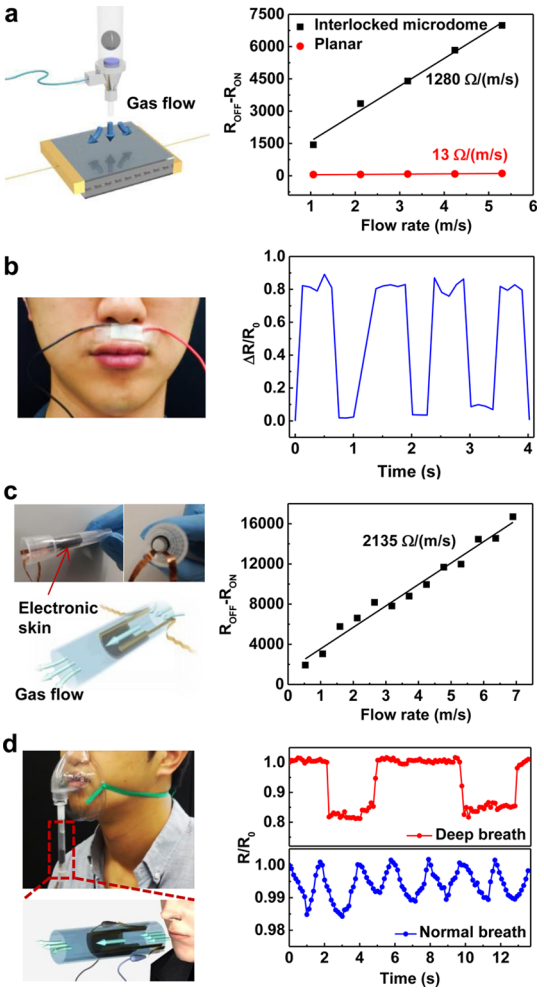

Figure 4. Monitoring of gas flow and human breathing. (a) Schematic of gas-flow sensing for planar-type electronic skins (left) and changes in resistance ($R_{off} - R_{on}$) as a function of flow rate for planar electronic skins (right). (b) Left: photograph of the planar-type flow sensors attached to the front of a volunteer's nostrils. Right: relative changes in resistance in response to human breathing. (c) Photographs of a tubular-type flow sensor composed of rolled-up electronic skin inside a plastic tube (upper left) and a schematic of a tubular-type gas flow sensor (bottom left). Right: relative changes in resistance as a function of flow rate. (d) Monitoring of human oral breathing. Left: photograph and schematic of tubular-type flow sensors integrated into the medical breathing mask for the monitoring of oral breathing. Right: relative changes in resistance for different oral breathing modes (deep and normal breathing) during periodic breathing.

13 Ω/m/s. We explored the potential for using our electronic skin to monitor human breathing in an experiment in which the electronic skin was attached to the front of the nostrils of a volunteer and the amount of air exhaled was measured (Figure 4b). The periodic breathing generates reliable and stable changes in resistance. Each exhalation event results in an 80% change in resistance.

For the analysis of oral breathing, we wrapped our electronic skins into a tube shape and monitored gas or breath flow (Figure 4c). The resistance of the tubular electronic skins increased linearly with the amount of

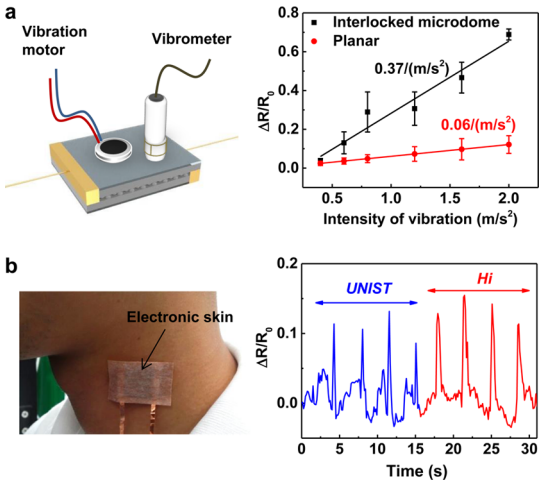

Figure 5. Vibration detection for wearable voice-monitoring systems. (a) Left: schematic of the vibration measurement. A coin-type vibration motor is used to generate vibration signals, and a vibrometer is used to measure the vibration intensity. Right: relative changes in resistance ($\Delta R/R_0$) as a function of vibration intensity. (b) Photograph of the electronic skin attached to a human neck for voice monitoring (right). Relative changes in resistance in response to different voices saying "UNIST" (blue) and "hi" (red).

air flowing through it, with a sensitivity of 2135 Ω/m/s. This sensitivity is about 1.7 times higher than that of planar-shaped sensors (1280 Ω/m/s) and significantly higher than that of flow sensors previously reported for conductive composite microcantilevers (66 Ω/m/s),[34] silicon microcantilevers (150−350 Ω/m/s),[35] and silicon nanowires (198 Ω/m/s).[36] The higher sensitivity of tubular electronic skin compared to the planar one can be attributed to the difference in effective pressure applied on each sensor. For the tubular sensor, the gas flow is confined and guided by the tubular path, which results in higher effective pressure than that for the planar sensor, where some amounts of gas flow out of the regulator diffuse in the other direction, resulting in reduced effective pressure. For demonstration purposes, the tubular flow sensor was also integrated into a medical breathing mask to monitor oral breathing (Figure 4d). The sensor can monitor different breathing modes (deep and normal breathing) with consistent changes in resistance under repeated breathing. Because our sensors are based on cost-effective and simple designs, they could be well suited as breathing sensors in cardiorespiratory monitoring, medical diagnosis, and rehabilitation.

As a final demonstration, we explored the potential use of our piezoresistive sensors for picking up vibrations, specifically those associated with speaking. Voice monitoring systems are critical for the clinical assessment of voice hyperfunction and disorders, as well as in electro-larynx devices.[37] Voice monitoring is typically performed using accelerometer-based devices.[37,38] To test the ability of our electronic skins to pick up voice vibrations, we attached a coin-type vibration motor to the interlocked films and placed a vibrometer in contact with the film to measure the vibration intensity (Figure 5a). The relative resistance of our sensor shows a linear increase with vibration intensity and a sensitivity of ~0.37/(m/s^2), which is significantly higher than the sensitivity of 0.06/(m/s^2) associated with planar composite films (Figure 5a). For use in wearable voice-monitoring systems, the sensors can be attached to the skin of the neck to monitor the voice directly. The sensors distinctly discriminate the different vibration patterns produced when the words "UNIST" and "hi" are spoken. Further optimization of the sensor design in combination with radiofrequency devices may enable wireless communication systems that avoid noise disturbance.

CONCLUSIONS

In conclusion, we have developed an electronic skin that consists of a CNT-composite-based elastomer film featuring interlocked microdome arrays, which lead to the giant tunneling piezoresistance and thus the high pressure sensitivity. The materials design and operational principles introduced here present a robust technology platform to further advance the sensitivity and response time of conventional composite elastomers for various sensor applications. The interlocked microdome arrays presented in this study are far from an ideal interlocked geometry, where all of the top microdomes are located in the central position of interstitial space between bottom microdomes, enabling the maximum variation of contact area for an applied pressure. Therefore, further optimization of alignment and position of top and bottom microdome arrays in the interlocked geometry will be required to fully utilize the unique design of interlocked microdome arrays and improve the sensitivity of electronic skins. We also anticipate that other types of filler materials and geometry of microstructures could expand the current-sensing capabilities to enable electronic skins with new functionalities. In addition, when integrated with other types of sensors and active electronic devices, the current platform could be a key component for the development of multifunctional electronic skin for applications in medical diagnostic tools and wearable human-health monitoring systems. Finally, the extreme resistance-switching behavior demonstrated here could enable highly efficient piezotronic transistors.[39,40]

EXPERIMENTAL SECTION

Elastomeric Composite Films with Microdome Arrays. For the fabrication of the precured CNT−PDMS composite mixtures, multiwalled nanotubes (MWNTs, Sigma Aldrich) with diameters ranging from 110 to 190 nm and lengths ranging from 5 to 9 μm were dispersed in chloroform by sonication for 6 h.

The dispersed MWNT solution was completely mixed with a PDMS base (Sylgard 184, Dow Corning) using a vortex mixer. Chloroform was subsequently removed by evaporation for 6 h at 90 °C on a hot plate. Immediately prior to the micromolding process, hexane and the PDMS curing agent (1:10 ratio for curing agent to base) were added to the dried MWNT−PDMS composite mixtures (at a ratio of 1 mL of hexane for each 500 mg of PDMS) and mixed with a vortex mixer for 5 min. For the fabrication of composite microdome arrays, the composite mixture was cast onto a silicon micromold with periodic hole arrays (dimensions: 3.5 μm diameter, 6 μm pitch, and 1 cm × 1.5 cm surface area) and thermally cured at 90 °C for 3 h. The silicon micromolds were purchased from KAIST National Nanofab Center. The thicknesses of the composite films were controlled to be ~500 μm. For the fabrication of the sensor arrays, platinum electrode lines with widths of ~5 mm were deposited on thin PDMS films (~500 μm) by sputter coating (EMITECH, K575X). The interlocked composite films were sandwiched between two PDMS films with platinum electrode lines. The tubular-type flow sensors were fabricated by inserting the interlocked films into micropipet tips (with a diameter of 1.2 cm and length of 5 cm).

Characterization. The microstructures of the composites were characterized using a field-emission scanning-electron microscope (SEM) (S-4800, Hitachi). The sheet resistance of the planar composite films was measured using a four-point-probe method (4200-SCS, Keithley). The change in electrical resistance of the microdome-patterned composites under various force conditions was measured using a two-probe method in which copper tapes were attached to each side of the microdome-patterned composite with silver paste and annealed at 100 °C for 1 h. The applied voltage for the resistance measurement is 10 V except for the measurement of Figures 2g and S6, in which we used 1 V for the comparison with the theoretical calculation of tunneling resistance. A home-built microstage system (Micro Motion Technology, Korea) was used to apply normal forces to the composite films, and a weight balance underneath was used to measure the forces. To evaluate the flow-detection capability, the skin sensors were exposed to argon flow (ranging from 1 to 5.3 m/s). The skin's vibration-detection capability was measured using a coin-type vibration motor (DVM1034, Motorbank Co., Korea) that controlled the intensity of the vibrations (0−2 m/s^2) and a vibrometer (ACO 3116, Guangzhou Orimay Electronic Co., Japan) that picked up the vibration intensities. The Young's moduli of composites were measured by tensile testing (universal testing machine, WL2100, WITHLAB Co., Korea) at a speed of 5 mm/min.

Finite-Element Method. In the contact-area calculations, we performed structural analyses using finite-element simulations. We modeled composites that were reinforced by different weight percentages of CNTs as linear elastic materials using experimentally measured elastic constants (Figure S8). Periodic boundary conditions were applied to the in-plane directions, and the bottom surface was fixed. All loading conditions were assigned through displacement control and converted to the corresponding pressure from reacting forces. We used more than 2.8 million four-node linear tetrahedral elements with an adaptive mesh-refinement scheme around the contact area. To model the mechanical contact between two deformable surfaces, a surface-to-surface contact scheme was employed.

Conflict of Interest: The authors declare no competing financial interest.

Supporting Information Available: Calculation of tunneling resistances, percolation threshold of CNT composites, and supplementary figures. This material is available free of charge *via* the Internet at http://pubs.acs.org.

Acknowledgment. This work was supported by the National Research Foundation of Korea (NRF-2011-0014965, NRF-2012-K1A3A1A20031618), BK21 Plus Program (10Z20130011057), Korea Institute of Machinery & Materials (KIMM) (NK175B), and Korea Institute of Science and Technology (KIST) (2E22112-11-249).

REFERENCES AND NOTES

1. Lumpkin, E. A.; Caterina, M. J. Mechanisms of Sensory Transduction in the Skin. *Nature* **2007**, *445*, 858–865.
2. Maheshwari, V.; Saraf, R. Tactile Devices to Sense Touch on a Par with a Human Finger. *Angew. Chem., Int. Ed.* **2008**, *47*, 7808–7826.
3. Dahiya, R. S.; Metta, G.; Valle, M.; Sandini, G. Tactile Sensing-From Humans to Humanoids. *IEEE Trans. Robot.* **2010**, *26*, 1–20.
4. Sekitani, T.; Yokota, T.; Zschieschang, U.; Klauk, H.; Bauer, S.; Takeuchi, K.; Takamiya, M.; Sakurai, T.; Someya, T. Organic Nonvolatile Memory Transistors for Flexible Sensor Arrays. *Science* **2009**, *326*, 1516–1519.
5. Takei, K.; Takahashi, T.; Ho, J. C.; Ko, H.; Gillies, A. G.; Leu, P. W.; Fearing, R. S.; Javey, A. Nanowire Active-Matrix Circuitry for Low-Voltage Macroscale Artificial Skin. *Nat. Mater.* **2010**, *9*, 821–826.
6. Mannsfeld, S. C. B.; Tee, B. C. K.; Stoltenberg, R. M.; Chen, C. V. H. H.; Barman, S.; Muir, B. V. O.; Sokolov, A. N.; Reese, C.; Bao, Z. N. Highly Sensitive Flexible Pressure Sensors with Microstructured Rubber Dielectric Layers. *Nat. Mater.* **2010**, *9*, 859–864.
7. Kim, D. H.; Lu, N. S.; Ghaffari, R.; Kim, Y. S.; Lee, S. P.; Xu, L. Z.; Wu, J. A.; Kim, R. H.; Song, J. Z.; Liu, Z. J.; *et al*. Materials for Multifunctional Balloon Catheters with Capabilities in Cardiac Electrophysiological Mapping and Ablation Therapy. *Nat. Mater.* **2011**, *10*, 316–323.
8. Yamada, T.; Hayamizu, Y.; Yamamoto, Y.; Yomogida, Y.; Izadi-Najafabadi, A.; Futaba, D. N.; Hata, K. A Stretchable Carbon Nanotube Strain Sensor for Human-Motion Detection. *Nat. Nanotechnol.* **2011**, *6*, 296–301.
9. Lipomi, D. J.; Vosgueritchian, M.; Tee, B. C. K.; Hellstrom, S. L.; Lee, J. A.; Fox, C. H.; Bao, Z. N. Skin-Like Pressure and Strain Sensors Based on Transparent Elastic Films of Carbon Nanotubes. *Nat. Nanotechnol.* **2011**, *6*, 788–792.
10. Pang, C.; Lee, G. Y.; Kim, T. I.; Kim, S. M.; Kim, H. N.; Ahn, S. H.; Suh, K. Y. A Flexible and Highly Sensitive Strain-Gauge Sensor Using Reversible Interlocking of Nanofibres. *Nat. Mater.* **2012**, *11*, 795–801.
11. Tee, B. C. K.; Wang, C.; Allen, R.; Bao, Z. N. An Electrically and Mechanically Self-Healing Composite with Pressure- and Flexion-Sensitive Properties for Electronic Skin Applications. *Nat. Nanotechnol.* **2012**, *7*, 825–832.
12. Persano, L.; Dagdeviren, C.; Su, Y. W.; Zhang, Y. H.; Girardo, S.; Pisignano, D.; Huang, Y. G.; Rogers, J. A. High Performance Piezoelectric Devices based on Aligned Arrays of Nanofibers of Poly(vinylidenefluoride-co-trifluoroethylene). *Nat. Commun.* **2013**, *4*, 1633–1643.
13. Webb, R. C.; Bonifas, A. P.; Behnaz, A.; Zhang, Y. H.; Yu, K. J.; Cheng, H. Y.; Shi, M. X.; Bian, Z. G.; Liu, Z. J.; Kim, Y. S.; *et al*. Ultrathin Conformal Devices for Precise and Continuous Thermal Characterization of Human Skin. *Nat. Mater.* **2013**, *12*, 938–944.
14. Wang, C.; Hwang, D.; Yu, Z. B.; Takei, K.; Park, J.; Chen, T.; Ma, B. W.; Javey, A. User-Interactive Electronic Skin for Instantaneous Pressure Visualization. *Nat. Mater.* **2013**, *12*, 899–904.
15. Schwartz, G.; Tee, B. C. K.; Mei, J. G.; Appleton, A. L.; Kim, D. H.; Wang, H. L.; Bao, Z. N. Flexible Polymer Transistors with High Pressure Sensitivity for Application in Electronic Skin and Health Monitoring. *Nat. Commun.* **2013**, *4*, 1859–1866.
16. Wu, W. Z.; Wen, X. N.; Wang, Z. L. Taxel-Addressable Matrix of Vertical-Nanowire Piezotronic Transistors for Active and Adaptive Tactile Imaging. *Science* **2013**, *340*, 952–957.
17. Fan, F. R.; Lin, L.; Zhu, G.; Wu, W. Z.; Zhang, R.; Wang, Z. L. Transparent Triboelectric Nanogenerators and Self-Powered Pressure Sensors Based on Micropatterned Plastic Films. *Nano Lett.* **2012**, *12*, 3109–3114.
18. Ruschau, G. R.; Yoshikawa, S.; Newnham, R. E. Resistivities of Conductive Composites. *J. Appl. Phys.* **1992**, *72*, 953–959.
19. Hu, N.; Karube, Y.; Yan, C.; Masuda, Z.; Fukunaga, H. Tunneling Effect in a Polymer/Carbon Nanotube Nanocomposite Strain Sensor. *Acta Mater.* **2008**, *56*, 2929–2936.

20. Bloor, D.; Donnelly, K.; Hands, P. J.; Laughlin, P.; Lussey, D. A Metal-Polymer Composite with Unusual Properties. *J. Phys. D: Appl. Phys.* **2005**, *38*, 2851–2860.
21. Mahmoud, W. E.; El-Lawindy, A. M. Y.; El Eraki, M. H.; Hassan, H. H. Butadiene Acrylonitrile Rubber Loaded Fast Extrusion Furnace Black as a Compressive Strain and Pressure Sensors. *Sens. Actuat. A* **2007**, *136*, 229–233.
22. Zhang, J.; Zhang, S. Y.; Feng, S. Y.; Jiang, Z. G. The Correlativity of Positive Temperature Coefficient Effects in Conductive Silicone Rubber. *Polym. Int.* **2005**, *54*, 1175–1179.
23. Alamusi; Hu, N.; Fukunaga, H.; Atobe, S.; Liu, Y. L.; Li, J. H. Piezoresistive Strain Sensors Made from Carbon Nanotubes Based Polymer Nanocomposites. *Sensors* **2011**, *11*, 10691–10723.
24. Stassi, S.; Canavese, G. Spiky Nanostructured Metal Particles as Filler of Polymeric Composites Showing Tunable Electrical Conductivity. *J. Polym. Sci., Part B: Polym. Phys.* **2012**, *50*, 984–992.
25. Copel, M.; Kuroda, M. A.; Gordon, M. S.; Liu, X. H.; Mahajan, S. S.; Martyna, G. J.; Moumen, N.; Armstrong, C.; Rossnagel, S. M.; Shaw, T. M.; *et al*. Giant Piezoresistive On/Off Ratios in Rare-Earth Chalcogenide Thin Films Enabling Nanomechanical Switching. *Nano Lett.* **2013**, *13*, 4650–4653.
26. Yao, H.-B.; Ge, J.; Wang, C. F.; Wang, X.; Hu, Z.; Zheng, Z.-J.; Ni, Y.; Yu, S.-H. A Flexible and Highly Pressure-Sensitive Graphene-Polyurethane Sponge. *Adv. Mater.* **2013**, *25*, 6692–6698.
27. Johansson, R. S.; Flanagan, J. R. Coding and Use of Tactile Signals from the Fingertips in Object Manipulation Tasks. *Nat. Rev. Neurosci.* **2009**, *10*, 345–359.
28. Ramuz, M.; Tee, B. C. K.; Tok, J. B. H.; Bao, Z. N. Transparent, Optical, Pressure-Sensitive Artificial Skin for Large-Area Stretchable Electronics. *Adv. Mater.* **2012**, *24*, 3223–3227.
29. Simmons, J. G. Generalized Formula for Electric Tunnel Effect between Similar Electrodes Separated by a Thin Insulating Film. *J. Appl. Phys.* **1963**, *34*, 1793–1803.
30. Archard, J. F. Elastic Deformation and the Laws of Friction. *Proc. R. Soc. London. Ser. A* **1957**, *243*, 190–205.
31. Braun, P. X.; Gmachl, C. F.; Dweik, R. A. Bridging the Collaborative Gap: Realizing the Clinical Potential of Breath Analysis for Disease Diagnosis and Monitoring-Tutorial. *IEEE J. Sens.* **2012**, *12*, 3258–3270.
32. Hedrich, F.; Kliche, K.; Storz, M.; Billat, S.; Ashauer, M.; Zengerle, R. Thermal Flow Sensors for MEMS Spirometric Devices. *Sens. Actuat. A* **2010**, *162*, 373–378.
33. Andre, N.; Druart, S.; Gerard, P.; Pampin, R.; Moreno-Hagelsieb, L.; Kezai, T.; Francis, L. A.; Flandre, D.; Raskin, J. P. Miniaturized Wireless Sensing System for Real-Time Breath Activity Recording. *IEEE J. Sens.* **2010**, *10*, 178–184.
34. Aiyar, A. R.; Song, C.; Kim, S. H.; Allen, M. G. An All-Polymer Airflow Sensor Using a Piezoresistive Composite Elastomer. *Smart Mater. Struct.* **2009**, *18*, 115002.
35. Zhang, Q.; Ruan, W.; Wang, H.; Zhou, Y.; Wang, Z.; Liu, L. A Self-Bended Piezoresistive Microcantilever Flow Sensor for Low Flow Rate Measurement. *Sens. Actuat. A* **2010**, *158*, 273–279.
36. Zhang, S. S.; Lou, L.; Lee, C. Piezoresistive Silicon Nanowire Based Nanoelectromechanical System Cantilever Air Flow Sensor. *Appl. Phys. Lett.* **2012**, *100*, 023111.
37. Mehta, D. D.; Zanartu, M.; Feng, S. W.; Cheyne, H. A.; Hillman, R. E. Mobile Voice Health Monitoring Using a Wearable Accelerometer Sensor and a Smartphone Platform. *IEEE Trans. Biomed. Eng.* **2012**, *59*, 3090–3096.
38. Nolan, M.; Madden, B.; Burke, E. Accelerometer Based Measurement for the Mapping of Neck Surface Vibrations during Vocalized Speech. *Annu. Int. Conf. IEEE* **2009**, 4453–4456.
39. Newns, D. M.; Elmegreen, B. G.; Liu, X. H.; Martyna, G. J. High Response Piezoelectric and Piezoresistive Materials for Fast, Low Voltage Switching: Simulation and Theory of Transduction Physics at the Nanometer-Scale. *Adv. Mater.* **2012**, *24*, 3672–3677.
40. Han, W. H.; Zhou, Y. S.; Zhang, Y.; Chen, C. Y.; Lin, L.; Wang, X.; Wang, S. H.; Wang, Z. L. Strain-Gated Piezotronic Transistors Based on Vertical Zinc Oxide Nanowires. *ACS Nano* **2012**, *6*, 5736–5736.